1-1-2019

Scalable honeycomb top contact to increase the light absorption and reduce the series resistance of thin film solar cells

Mehdi Sadatgol
Michigan Technological University

Nupur Bihari
Michigan Technological University

Joshua M. Pearce
Michigan Technological University

Durdo O. Guney
Michigan Technological University

Recommended Citation

Sadatgol, M., Bihari, N., Pearce, J. M., & Guney, D. O. (2019). Scalable honeycomb top contact to increase the light absorption and reduce the series resistance of thin film solar cells. *Optical Materials Express, 9*(1), 256-268. http://dx.doi.org/10.1364/OME.9.000256
Retrieved from: https://digitalcommons.mtu.edu/ece_fp/46

Follow this and additional works at: https://digitalcommons.mtu.edu/ece_fp

 Part of the Engineering Commons

Research Article | Vol. 9, No. 1 | 1 Jan 2019 | OPTICAL MATERIALS EXPRESS 256
Optical Materials EXPRESS

Scalable honeycomb top contact to increase the light absorption and reduce the series resistance of thin film solar cells

MEHDI SADATGOL,[1,*] NUPUR BIHARI,[2] JOSHUA M. PEARCE,[1,2] AND DURDU O. GUNEY[1]

[1]*Department of Electrical and Computer Engineering, Michigan Technological University, Houghton, MI, USA*
[2]*Department of Material Science and Engineering, Michigan Technological University, Houghton, MI, USA*
**sadatgol@mtu.edu*

Abstract: This paper presents a novel design for the top contact of thin film photovoltaic (PV) solar cells. The new top contact is formed by fabricating a 20nm thin honeycomb shaped silver mesh on top of an ultra-thin 13nm of indium tin oxide. The new top contact offers the potential to reduce the series resistance of the cell while increasing the light current via plasmonic resonance. Using the nano-bead lithography technique the honeycomb top contact was fabricated and electrically characterized. The experimental results verified the new contact reduces the sheet resistance by about 40%. Numerical simulations were then used to analyze the potential performance enhancement in the cell. The results suggest the proposed top contact integrated with a typical thin film hydrogenated amorphous silicon PV device would lead to more than an 8% improvement in the overall efficiency of the cell.

1. Introduction

The ever-growing demand for energy along with the negative environmental impacts and increasing costs of fossil fuels, have motivated the scientific community to explore inexpensive, clean and renewable sources of energy [1]. Solar photovoltaic (PV) technology, which converts light directly to electricity, is one of the most appealing alternatives to sustainably supply the increasing global electrical energy demand [2]. PV costs have steadily declined [3,4] and now represent the fastest growing source of electricity, however, costs must continue to decline for the levelized cost of solar electricity [5] to eliminate the need for traditional electricity sources and their externalities in their entirety. Besides cost savings in material selections and fabrication process efficiencies, improvement in the conversion efficiency of solar cells cuts the total expense of solar PV deployment by reducing the number of modules required to deliver given amount of electric power and thus the concomitant labor and balance of systems (BOS) expenses such as land and racking materials. Thin film hydrogenated amorphous silicon (a-Si:H) solar cells are an important example of potentially useful means to economically fabricate PV. Cost effective plasma enhanced chemical vapor deposition (PECVD) and low material usage made the thin film a-Si:H solar cell appealing for the replacement of single crystal and polycrystalline solar cells. However, thin film a-Si:H cells are not as efficient as their crystalline and polycrystalline counterparts. The highest confirmed efficiency for thin film a-Si is about 11% (12% if a tandem microcrystalline layer is used), which is about half of the efficiency of crystalline Si solar cells [6].

Several researchers have used innovation in plasmonics to increase the efficiency of thin film a-Si:H solar cells. For example, Derkacs and associates increased the short circuit current density of thin film a-Si:H solar cells with forward scattering by surface plasmon polariton modes [7]. Spinelli and colleagues modified the back reflector with plasmonic silver nano-

#348273 https://doi.org/10.1364/OME.9.000256
Journal © 2019 Received 15 Oct 2018; revised 21 Nov 2018; accepted 4 Dec 2018; published 19 Dec 2018

Optical Materials EXPRESS

particles to enhance light absorption through light-trapping [8]. Aydin et al. proposed a thin plasmonic absorber consisting of a metal–insulator–metal stack with a nano-structured top silver film to increase the light absorption [9]. Massoit and associates used one dimensional array of silver strips to form a broadband light trapping mechanism in order to enhance the light absorption of the cell [10]. Zhang et al., found improved a-Si:H PV device performance with an enhanced front-surface hexagonal plasmonic arrays made from nano-scale lithography [11]. These approaches are promising and this study aims to further those efforts by analyzing a new top contact that is able to be manufactured economically at a large scale. Beside plasmonic, in this paper, we propose a new design for thin film a-Si:H with a unique top emitter layer. We report a series of experiments and measurements to demonstrate feasibility of implementation for the proposed emitter layer. In addition, we run numerical simulations to reveal the potential for the new top emitter layer to increase the efficiency of a-Si:H-based PV cells by quantifying the enhancement of light absorption in the active region and the reduction in the series resistance.

2. Plasmonic thin film a-Si:H solar cell

A typical thin film a-Si:H solar cell consists of several semiconductor and conductive layers with different thicknesses as is shown in Fig. 1. The thickness and optical properties of these layers especially the top transparent conductive oxides (TCO) and intrinsic a-Si:H layer have a strong impact on the optical properties of the cell. The intrinsic a-Si:H is the active region of the cell and produces the photocurrent generated by the cell. However, absorption of light in the active a-Si:H layer drops drastically as the wavelength of light increases beyond 600nm. As a result, most of the light energy at large wavelength regions ($\lambda > 600$nm), is not harvested by the cell. For the short wavelength region ($\lambda < 450$nm), on the other hand, the incident light mostly dissipates in the p-type amorphous silicon layer and does not reach the active layer. Considering these two effects, the cell is more efficient within the $450\text{nm} < \lambda < 600\text{nm}$ window. Therefore, it is essential to maximize the transmission of sunlight within the $450\text{nm} < \lambda < 600\text{nm}$ window into the active layer. This explains the need for adding an anti-reflection coating (ARC) on top of the cell, which reduces the reflection and increases the transmission in the $450\text{nm} < \lambda < 600\text{nm}$ window. The TCO layer, which is normally made out of indium tin oxide (ITO), serves as the ARC. TCOs were initially integrated with thin film solar cells to reduce the series resistance of the cells by lowering the sheet resistance of the emitter layer [12]. However, in modern cells TCO layer has multiple functionalities such as barrier to prevent the back reflector (BR) and top grid metal to diffuse inside the active layer [13], and the ARC as mentioned.

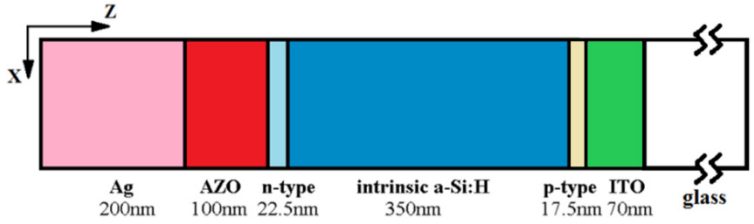

Fig. 1. Cross section of a typical thin film a-Si:H solar cell. From right, white is the glass superstrate, gray is the top TCO layer made of thin film indium thin oxide (ITO), green is p-type amorphous silicon, deep blue is intrinsic a-Si:H, light blue is n-type amorphous silicon, red is the bottom TCO layer made of aluminum zinc oxide (AZO), and pink is the bottom layer made out of silver.

Although the ARC is beneficial for the $450\text{nm} < \lambda < 600\text{nm}$ window, it rejects the incident light at higher wavelengths, $\lambda > 650$nm. The low absorption of the active layer along with the high reflection of incident light by the ARC result in poor efficiency for the large wavelength region. Plasmonic nano-structures were recently exploited to alleviate the low efficiency of

Optical Materials EXPRESS

thin film a-Si:H cells in the large wavelength region [14,15]. The strong interaction of the plasmonic particles with the incident light results in diffraction and local field enhancement among other phenomena. Change in the direction of propagation of the light due to diffraction reduces the reflection caused by ARC in the large wavelength region. At the same time, it increases the light path length in the active layer since it propagates at an oblique angle. As an example, Vora et al. reported 20% enhancement in the light current in a-Si:H solar cell by adding nano-disks on top of ITO layer [14]. For further details, readers can see the review article by Atwater and associates that summarizes several different designs and configurations along with the underlying working mechanism of the plasmonic solar cells [15]. In order to make this approach more effective, one needs to reduce the thickness of the TCO layer. Consequently, the sheet resistance of the emitter layer increases, which in turn leads to an increase in the series resistance of the cell [16,17]. The short circuit current (I_{SC}) and fill factor (FF) of the solar cell reduces, as the series resistance gets larger, which both contribute to a decrease in overall cell conversion efficiency. Therefore, the maximum power (MP) delivered by the cell may reduce despite the improvement in absorption and light current. Increasing the diffraction and light absorption by texturing the AZO and intrinsic layers has been exploited and around 26% increase in the efficiency was reported using this method [18–20]. Nevertheless, the plasmonic approach could be applied to textured cells as well to further increase the efficiency. Besides, the plasmonic approach is not limited only to a-Si:H solar cells and it could be applied to a wide variety of thin-film solar cells including GaAs and polymer solar cells [21,22].

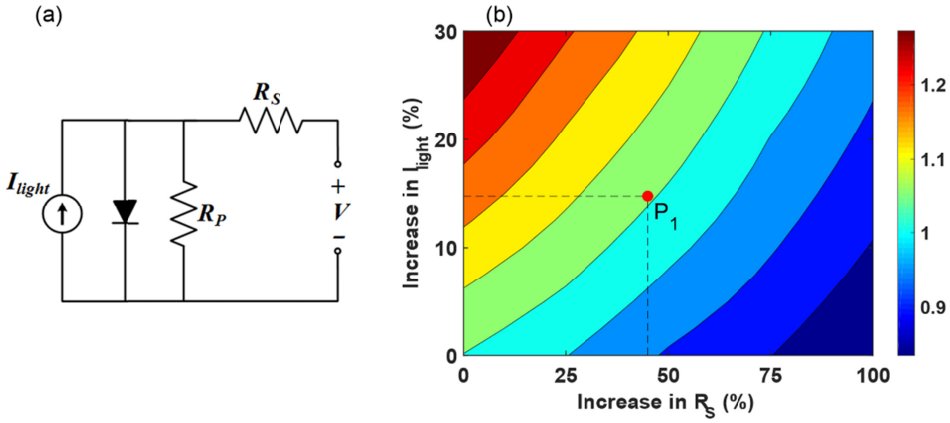

Fig. 2. (a) Five-parameter model for solar cell. (b) Change in MPP as I_{light} increases from 0 to 30% and R_S increases from 0 to 100% for the typical thin film a-Si:H solar cell with V_{OC} = 1.3V, I_{SC} = 1.3A, I_0 = 0.31nA, η = 1.36, R_S = 0.2Ω and R_P = 6.3Ω. The point P_1 corresponds to 15% increase in I_{light} and 43% increase in the R_S.

We have performed a numerical study to explore the combined effect of the series resistance, R_S, and the light current, I_{light}, on the overall efficiency of thin film a-Si:H solar cells. The maximum power point (MPP) under the standardized conditions of 1 sun with an air mass of 1.5 (AM1.5) is considered to be the metric for the overall efficiency. The five-parameter model shown in Fig. 2(a) which consists of a current source, a diode, a series resistance and a parallel resistance is used for the calculation [23]. The result of the study for a typical thin film a-Si:H solar cell with open circuit voltage V_{OC} = 1.3V, short circuit current I_{SC} = 1.3A, reverse bias saturation current I_0 = 0.31nA, diode ideality factor η = 1.36, series resistance R_S = 0.2Ω and parallel resistance R_P = 6.3Ω is illustrated in Fig. 2(b). We should mention the values for the five-parameter model of the typical cell was obtained by averaging several commercial thin film a-Si:H solar cells listed in [24]. As Fig. 2(b) suggests, increases in series resistance could diminish any improvement gained in the light current by increasing

Optical Materials EXPRESS

the light absorption of the cell. For the high-level model, which is applicable to a wide range of cells, being used in our study for instance, a 15% increase in the light current has positive effect on the MPP only if the increase in the series resistance is less than 43% (see point P_1 in Fig. 2(b). Thus, it is crucial to keep the series resistance below some certain value while optimizing or redesigning a solar cell to increase the light absorption.

Inspired by this outcome, we designed a new plasmonic thin film a-Si:H cell that reduces the series resistance of the cell along with enhancement in the light absorption. The design which we refer to as the honeycomb emitter is shown in Fig. 3. The top contact of the new cell consists of a thin ITO layer that is partially covered by a silver mesh resembling a honeycomb. The 13nm ultra-thin ITO is set to form a low resistance ohmic junction with the active layer at the bottom [25] and prevent diffusion of the top silver mesh. The silver mesh provides a low resistance path to deliver the photo-generated current to the external terminal of the cell. As we elaborate in the next section, a properly designed honeycomb mesh improves light absorption in $\lambda > 650$nm region without deteriorating the performance of the cell in $450\text{nm} < \lambda < 600\text{nm}$. The honeycomb thin film solar cell is a periodic structure in the X and Y directions (see Fig. 3). Figure 3 shows 6 of the unit cells in a 3 by 2 arrangement. A thin metallic film with an array of subwavelength holes has been proposed before to improve the efficiency of organic solar cells [26]. However, the honeycomb pattern benefits from scalable and relatively low cost self-assembled nano-beads lithography technique [11,27–31]. In [32], the authors used nano-beads lithography to make a perforated metallic film which in turn could be used to lower the resistance of the top contact. However, the plasmonic resonance was not being considered. In addition, the authors only consider the metallic mesh by itself, not as a part of a solar cell.

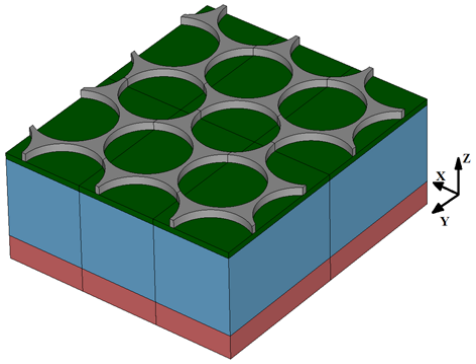

Fig. 3. Schematic of 6 unit cells of honeycomb thin film solar cell. The silver mesh is shown in grey. The top TCO layer is in green, active layer in blue, and the bottom TCO layer in red. The drawing is not to scale.

As the result of diffraction of the incident light by the silver mesh, the energy of incident light is distributed between the different diffracted orders. The amount of power in the non-zero diffracted orders to the total incident power is called diffraction efficiency, η_D. Larger the η_D, more of the energy of the incident light transfers to non-zero diffracted orders, which is desirable for increasing the light current at high wavelength region. Plasmonic resonance enables the silver mesh to enhance the η_D at a given frequency dependent on the geometry of the mesh. The thickness, radius of the opening and periodicity of the mesh determine the frequency and strength of the plasmonic resonance [33]. At the resonance frequency, electric and magnetic fields are very strong at the silver-ITO interface and decay rapidly as the distance to the interface increases; this phenomenon is called local field enhancement. The η_D increases as the result of the local field enhancement and Fourier

Optical Materials EXPRESS

expansion explains the connection between these two. Power in every diffracted order is proportional to the squared magnitude of the corresponding harmonic in the 2D Fourier expansion of electric and magnetic field. The fast and intense change in the fields as the result of local field enhancement leads to large harmonic content in the 2D Fourier expansion of the field, which in turn, means higher power in the non-zero diffracted orders.

3. Design, modeling, a of honeycomb top contact

Since this particular application requires high diffraction efficiency for $\lambda \geq 600\text{nm}$, the silver mesh was designed based on the guidelines provided in [33] to resonate at 600nm. The resonance frequency and diffraction efficiency were found form the numerical simulation. The COMSOL RF module, a commercially available full-wave electromagnetic simulation tool, was used to perform the numerical simulation. The result of the numerical modeling was used in an iterative fashion to tune the geometrical parameters of the silver mesh in order to achieve the desired resonance frequency.

In order to find the diffraction efficiency on the mesh, the electric and the magnetic fields were found numerically on a test plane on the top boundary of the intrinsic a-Si. Having the electric fields everywhere on the test plane, we can apply the Fourier integral to decompose the field into plane waves that propagate in the different directions, or the diffracted orders. The amplitudes of the X and Y polarized electric fields, $E_x^{m,n}$ and $E_y^{m,n}$, for all the different diffracted orders are given by

$$E_i^{m,n} = \frac{1}{WL} \iint\limits_{\substack{-\frac{W}{2}<x<\frac{W}{2} \\ -\frac{L}{2}<y<\frac{L}{2}}} E_i(x,y) e^{j\frac{m2\pi}{W}x} e^{j\frac{n2\pi}{L}y} dxdy \tag{1}$$

In Eq. (1), *i* represents the X and Y, and $E_i(x,y)$ is the *i* component of the electric field on the test plane found from simulation. *W* and *L* are the length of the unit cell in the X and Y directions, respectively (see Fig. 3). *m* and *n* denote the order of diffraction in the X and Y directions respectively. In other words, the X component of the wave vector is $m2\pi/W$ and the Y component is $n2\pi/L$.

Having the amplitude of every diffracted order, we can easily find the diffraction efficiency for the normally incident light. The sum of the powers in the all diffracted components is equal to the total power minus power in the undiffracted modes. Therefore, the diffraction efficiency could be written as

$$\eta_D = \frac{P_{output} - \frac{1}{|Z|}\left(\left|E_x^{0,0}\right|^2 + \left|E_y^{0,0}\right|^2\right)}{P_{incident}}. \tag{2}$$

In Eq. (2), *Z* denotes wave impedance of intrinsic a-Si:H layer, $P_{incident}$ is the incident power density, and P_{output} is the total power density passed the silver mesh.

After a couple of iterations, we found a silver mesh with thickness of 20nm, the diameter of the openings of 0.92μm, the periodicity (center-to-center distance between two adjacent openings) of 1μm resonates at 600nm. The ITO layer beneath the mesh is 13nm, because the 13nm ITO layer is not thick enough to work as an ARC for 450nm < λ <600nm, a 48nm thick layer of silicon nitride (Si_3N_4 or simply SiN) was added on top of the ITO layer. We selected SiN because it has refractive index value very close to the refractive index of ITO and is much less absorptive compared to ITO. In this design, the combination of 13nm ITO and 48nm SiN together acts as the modified ARC. Diffraction of light inside the ARC increases the light absorption through two different mechanisms. First, an obliquely propagating wave has a longer path length in the active layer, therefore absorption in the active layer increases. Second, if the angle of propagation for the diffracted light is greater than the critical angle for the total internal reflection at the air-ITO interface, the wave cannot escape back to the air.

Optical Materials EXPRESS

For the honeycomb solar cell, diffraction is the result of the interaction of light with the silver mesh embedded inside the modified ARC layer. Figure 4(a) shows the spectrum of the diffraction efficiency and dissipated power in the silver mesh for an X polarized normally incident light. The diffraction efficiency was calculated for the test plane inside the intrinsic a-Si layer, very close to the intrinsic and p-type a-Si:H interface (see Fig. 1). All the reflection from the bottom boundary of the a-Si layer was suppressed by adding a perfectly matched layer (PML) to the bottom boundary (PML was added only to calculate the diffraction efficiency). The peaks in the dissipated power corresponds with the plasmonic resonances of the silver net. As illustrated in Fig. 4(a), the diffraction efficiency increases at $\lambda = 600\text{nm}$, where the silver net has one of the resonances. Because of the 6-fold rotational symmetry of the honeycomb there is no polarization dependence for normally incident light. For the sake of simplicity only the X component of the electric field on the test plane at 600nm is shown in Fig. 4(b).

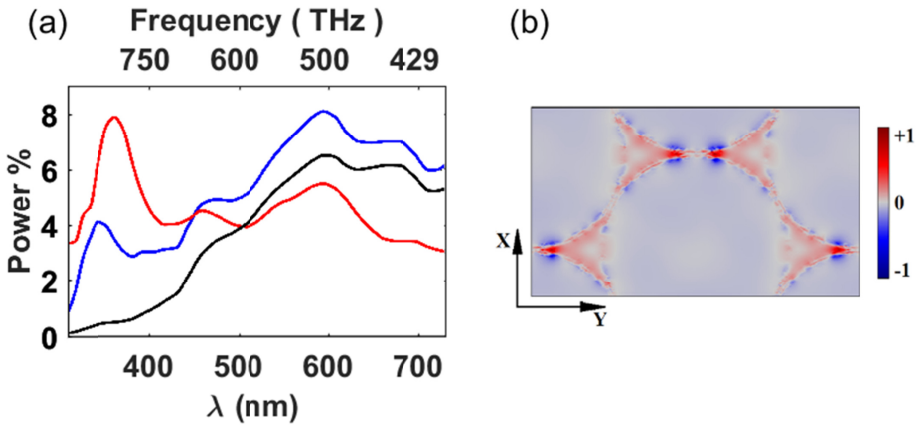

Fig. 4. (a) Black is the diffraction efficiency (Eq. (2), red is the dissipated power in the silver mesh, and blue is the output diffraction efficiency. (b) X component of the electric field (arbitrary unit) on the test plane at resonance $\lambda = 600nm$.

The spectrum of the dissipated power in the silver mesh (Fig. 4(a)) suggests there is another strong plasmonic resonance at $\lambda = 375nm$. However, there is no coincident increase in the diffraction efficiency at this frequency. This inconsistency could be attributed to the high absorption of the p-type a-Si layer. The diffraction efficiency in Fig. 4(a) was calculated on the test plane on top of the intrinsic a-Si layer. As mentioned earlier, the p-type a-Si layer which is located between the honeycomb mesh and the test plane is very absorptive for $\lambda < 400nm$. As a result, most of the power in this wavelength region is absorbed by the p-type layer and a small portion of the light reaches the test plane and consequently diffraction efficiency decreases. In order to further clarify this point, we define a new parameter called output diffraction efficiency as the ratio of transmitted power in the nonzero diffracted orders to the total transmitted power. The output efficiency calculated with the same test plane is shown in Fig. 4(a). As it is clear in the figure, the output diffraction efficiency has a peak close to $\lambda = 375nm$ which is the indication of a strong diffraction.

The numerical simulation was utilized to find the optical absorption in the active layer and photo-current for the complete honeycomb solar cell. Figure 5 shows the optical absorption spectra in the intrinsic a-Si:H layer (the active layer) for the honeycomb solar cell and the reference solar cell in Fig. 1, both for normally incident light under standardized condition of AM1.5. The honeycomb a-Si:H shows 7.5% increase in the optical absorption and 8% improvement in the photo-current compared to the reference a-Si:H solar cell. This is

Optical Materials EXPRESS

promising, but it is important to consider that the improvement in the optical absorption is not gained at the expense of an increase in the series resistance.

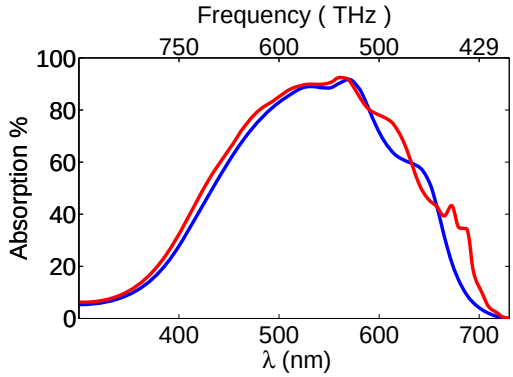

Fig. 5. Red shows the absorption spectra in the intrinsic a-Si:H layer of the honeycomb solar cell and blue shows absorption spectra for the reference a-Si:H solar cell under normally incident 1.5AM illumination for 300nm < λ <730nm.

Using the COMSOL model we found the absorption in the different layers of the honeycomb cell, the results are illustrated in Fig. 6(a). Since the absorption in the SiN and the n-type amorphous silicon layers were much lower compared to the absorption in the other layers we did not include them in the figure. As it was expected, the p-type amorphous silicon absorbs a noticeable portion of the incident light at the low-wavelength region. It is also worth mentioning that the absorption in the silver mesh incorporated with the a-Si:H solar cell is different from the absorption in the silver mesh shown in Fig. 4(a). The reason for this difference relies on the fact that the geometry which has been used to find the diffraction efficiency in Fig. 4(a) is different from the geometry for the complete solar cell. Additionally, the reflections from the honeycomb cell and the reference cell were calculated and are shown in Fig. 6(b). The honeycomb ARC consisting of SiN and ITO layers minimize the reflection for 450nm < λ <600nm region, while the resonances in the silver mesh reduce the excessive reflection outside this region.

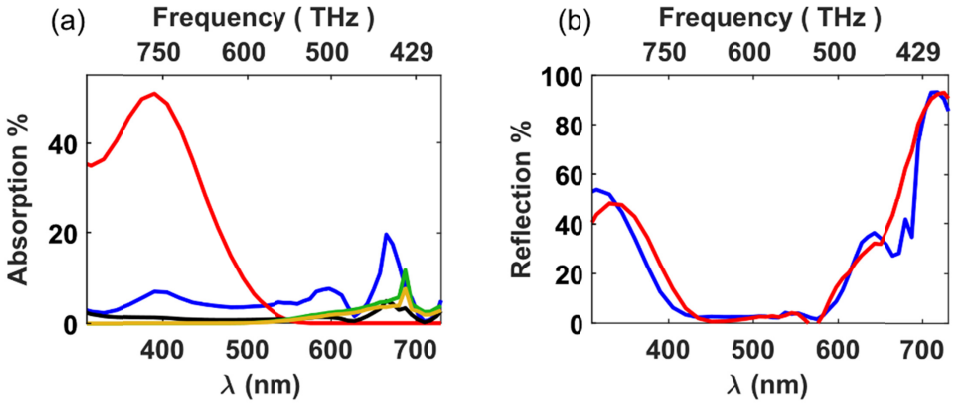

Fig. 6. (a) Absorption in different layers of the honeycomb solar cell. The red, blue, black, green, and yellow lines show the absorptions in the p-type a-Si layer, silver mesh, ITO, AZO, and the silver back reflector, respectively. (b) The blue line shows the reflected power from the honeycomb solar cell, while the red line shows the reflection from the reference cell.

The resistance of the emitter layer is one of the major contributors to the series resistance of a thin film solar cell. The other major contributors to the R_S are the junction resistances between top TCO and p-type a-Si and between bottom TCO and n-type a-Si layer [12,34].

Optical Materials EXPRESS

Clearly, one needs to first quantify the contribution of the different components of R_S in order to study the effect of emitter layer sheet resistance in the performance of the cell. The junction resistivity and the emitter sheet resistance depend strongly on the materials, technology and fabrication conditions. As a result, the contribution of emitter layer in the R_S varies from one solar cell to another one, and typically ranges from 10% to 30% [35,36]. This implies that if a modification on a cell doubles the emitter sheet resistance, the total series resistance would increase by 10-30%.

Sheet resistance of a flat uniform layer is given by ρ/t where ρ is the specific resistance and t is the thickness of the layer. For a 70nm thick ITO layer with specific resistance of $\rho_{ITO}=5\times10^{-6}\Omega m$ the sheet resistance is 71Ω/sq. For a complex structure like the honeycomb emitter layer it is essential to first define sheet resistance. A voltage drop is built as the photo generated current passes through the honeycomb emitter to reach the external terminals of the solar cell. We define the effective sheet resistance of the honeycomb emitter such that if the honeycomb emitter is replaced by a virtual layer with sheet resistance equal to the effective sheet resistance, then the voltage drop across the layer does not change. To find the effective sheet resistance, the scenario illustrated in Fig. 7 (the structure is assumed to be very long in the Y direction compared to the size of the structure in the X and Z directions) was considered. A uniform current density J is applied to the lower boundary of the ITO layer and the current is collected from a terminal attached to the top edge of the silver net. The SiN layer was not included in this analysis, because its resistance is orders of magnitude larger than the silver mesh and ITO layer [37]. The terminal is located at $x=0$, kept at zero potential and the terminal-silver mesh junction resistance is negligible. Voltage drop across a small distance between x and $x+\Delta x$ is equal to $\Delta V(x)=V(x+\Delta V)-V(x)=\sigma_e J(L-x)\Delta x$, where Δx is a small increment in the X direction, σ_e is the effective sheet resistance of the honeycomb emitter, and L is the length of the honeycomb emitter in the X direction. The potential at any arbitrary point on the honeycomb emitter is found to be:

$$V(x)=\frac{1}{2}\sigma_e Jx(2L-x) \tag{3}$$

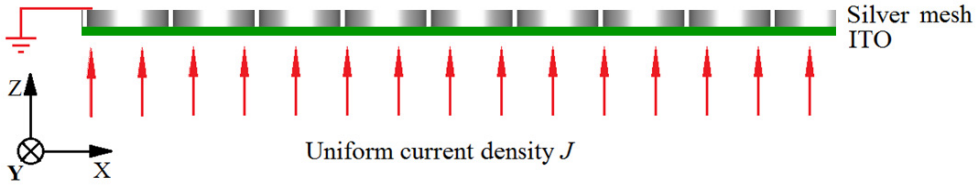

Fig. 7. The scenario to find the effective sheet resistance of honeycomb emitter layer (only a few unit cells of the honeycomb top contact are shown).

The structure in Fig. 7 has been studied numerically using the COMSOL AC/DC module to find the potential at any point on the honeycomb emitter layer. The specific resistivity of silver is considered to be $\rho_{Ag}=7\times10^{-8}\Omega m$ [38] and the specific resistivity of the 13nm thick ITO layer is $\rho_{ITO}=1.15\times10^{-5}\Omega m$ extrapolated form [39]. The silver mesh is 20nm thick and has openings with diameter 0.92μm and a separation of 1μm (center to center). The result of the numerical simulation is illustrated in Fig. 8.

Optical Materials EXPRESS

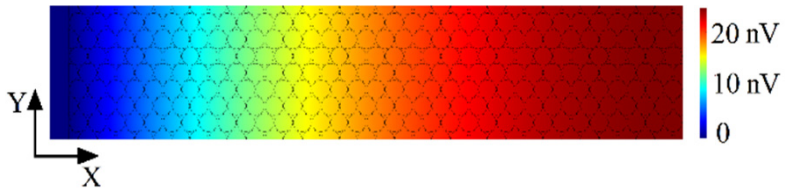

Fig. 8. Voltage drop across the honeycomb emitter layer in response to flow of uniform current density of $1 Am^{-2}$ (only part of the structure in the Y direction is shown).

The simulation result in Fig. 8 fits with the analytical model described in Eq. (3) with less than 1% mean squared error and results in a value of 42Ω/sq for the effective sheet resistance (~40% less than sheet resistance of the reference cell with 70nm ITO layer). Assuming 10-30% of the series resistance is from the emitter layer, the series resistance of the honeycomb a-Si:H solar is 4% to 12% less than the reference cell. For plasmonic solar cells with a thin layer of ITO and isolated metallic islands, the effective resistance of emitter layer increases several times. As an example, for the nano-disk plasmonic solar cell (NDPS) [14] the effective sheet resistance of the emitter layer is about 640Ω/sq, which is 9 times larger than the reference cell. Consequently, the series resistance of the NDPS is more than two times that of the reference cell.

4. Fabrication of the honeycomb silver mesh

A 13nm layer of ITO (In_2O_3/SnO_2 90/10 weight ratio) was deposited on silicon substrate using a Perkin Elmer 2400-6J RF sputtering system. Since the deposition rate on the system used was not characterized for sub 30nm films, experiments involving different RF powers and deposition times were completed. It was determined that a 15 second deposition with an RF power ramp rate of approximately $10 W/s$ resulted in a 13nm film. Here, the RF power was brought up to 100W in 10 seconds, and held constant for 5 seconds before turning the supply off. The film thickness was verified using a J. A. Woollam Vertical VASE ellipsometer and a 5-point scan was done to check for uniformity across the sample. A monolayer of polystyrene beads with average diameter of 1μm was then deposited on this ITO layer using methods described in [11,28]. A Veeco Dim 3000 (Plainview, NY) atomic force microscope (AFM) in tapping mode at 1 Hz was used to scan a 10 μm × 10 μm area. The AFM image in Fig. 9 shows the monolayer of the beads in a close packed configuration.

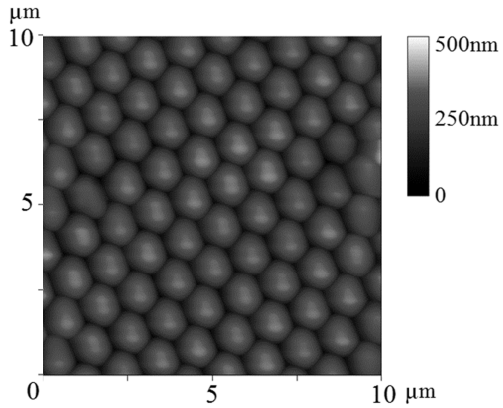

Fig. 9. AFM image of 1μm polystyrene beads in close packed configuration on 13nm ITO on glass substrate.

To create a mask for the silver mesh, the beads were etched in an oxygen plasma at RF power of 100W for 15 seconds using a March Jupiter II reactive ion etch (RIE). A process

Optical Materials EXPRESS

pressure of 200mTorr was maintained to ensure repeatability of process. Using a KH Frederick EB12 evaporator, a 20.5nm thick layer of silver was then deposited on top of the sample. A Hitachi S-4700 FE-SEM was used at 5kV to image the polystyrene beads after the oxygen plasma etch (Fig. 10(a)). Image analysis using a custom-built MATLAB script was performed to measure the spacing between each bead. It was concluded that an RIE power of 100W with an etch time of 15 seconds with 98 standard cubic centimeters per minute (SCCM) of oxygen would result in reduction in diameter of the beads by 8%. The beads were removed using a sonicated chloroform triple wash [40], leaving a silver mesh as shown in Fig. 10(b). Although theoretically the mesh pattern is considered to be uniform, when fabricating the devices in the real world, it is clear that there is a nonuniformity in the mesh pattern as shown in Fig. 9. These nonuniform meshes would be expected to under-perform what is projected from simulations, because, for example, constrictions where the channel width is reduced would result in a higher sheet resistance. However, the preliminary results shown here are promising enough that the necessary engineering work is encouraged to further optimize the fabrication of a uniform mesh in order to be able to get experimental results closer to those predicted by simulation.

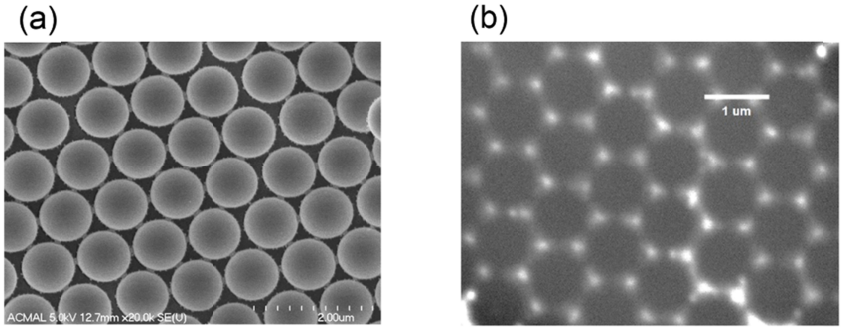

Fig. 10. (a) SEM image of polystyrene beads on a 13nm ITO on silicon substrate showing bead diameter reduction by 8%. (b) SEM image of the silver mesh on a 13nm ITO after removing the polystyrene beads.

Figure 11 shows the sheet resistance of the silver mesh on top of the ITO layer which was measured using an open-source automated mapping four-point probe (OS4PP) [41]. The variation in sheet resistance was attributed to the small size of the sample (approximately 1cm × 1cm), resulting in edge effects from the 4-point probe measurement. It was observed that the sheet resistance of the honeycomb silver mesh on ITO layer has average value of 33.22Ω/sq with standard deviation of 12.75Ω/sq. The difference from the simulated value of 42Ω/sq is attributed the small sample geometry, as well as the finite sheet resistance of the silicon substrate which is 154-308Ω/sq. However, having the simulated sheet resistance within the error of the measured value indicates that a 20.5nm thick silver mesh overlaid on a 13nm thick ITO layer has the capability to bring down the sheet resistance significantly.

Optical Materials EXPRESS

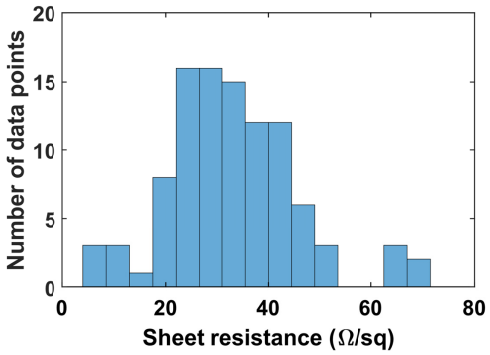

Fig. 11. Histogram of the measured sheet resistance for the honeycomb silver mesh structure on an ITO/Si substrate.

5. Conclusions

A new design consisting of a silver mesh with 20nm thickness and 13nm thin layer of ITO is proposed to replace the top contact of thin film solar cells. The effect of the new top contact was numerically studied on a-Si:H thin film solar cells. Beside reducing the series resistance, the silver mesh improves the light absorption of a cell via plasmonic resonance. A series of experiments were conducted to deposit the 13nm ITO layer and fabricate the silver mesh on top of the ultra-thin ITO layer. The successful fabrication of the top contact was verified with sheet resistant measurements. These ultra-thin TCO film is useful not only for depositing the top contact in photovoltaic cells but also have applications in sensor and diode fabrication [28,42,43]. Fabrication of an entire thin film solar cell with the honeycomb top contact and integration of the method with commercial a-Si:H thin film solar cell fabrication process can further prove the merit of the new design.

Funding

National Science Foundation (CBET-1235750).

Acknowledgments

The authors acknowledge the efforts of Sandra Cvetanović for bead deposition and Ameya Narkar for their chemical removal. The authors acknowledge the Applied Chemical & Morphological Analysis Laboratory at Michigan Tech for use of the instruments and staff assistance. Parts of this study were completed using Michigan Technological University's Microfabrication Facility. Portions of this work were presented in “Sadatgol, Mehdi, Exotic optical properties of metal-dielectric nano-structures,” PhD diss., Michigan Technological University, 2016.

References

1. U.S. Energy Information Administration (EIA), “The Annual Energy Outlook 2015 (AEO2015).” Available at: http://www.eia.gov/forecasts/aeo/pdf/0383%282015%29.pdf, (Accessed on 12th June 2016).
2. J. M. Pearce, “Photovoltaics—a path to sustainable futures,” Futures **34**(7), 663–674 (2002).
3. C. Candelise, M. Winskel, and R. J. K. Gross, “The dynamics of solar PV costs and prices as a challenge for technology forecasting,” Renew. Sustain. Energy Rev. **26**, 96–107 (2013).
4. U. Pillai, “Drivers of Cost Reduction in Solar photovoltaic,” Energy Econ. **50**, 286–293 (2015).
5. K. Branker, M. J. M. Pathak, and J. M. Pearce, “A Review of Solar Photovoltaic Levelized Cost of Electricity,” Renew. Sustain. Energy Rev. **15**(9), 4470–4482 (2011).
6. M. A. Green, Y. Hishikawa, E. D. Dunlop, D. H. Levi, J. Hohl-Ebinger, and A. W. Y. Ho-Baillie, “Solar cell efficiency tables (version 50).” Progress in Photovoltaics 26, no. NREL (2017).
7. D. Derkacs, S. H. Lim, P. Matheu, W. Mar, and E. T. Yu, “Improved performance of amorphous silicon solar cells via scattering from surface plasmon polaritons in nearby metallic nanoparticles,” Appl. Phys. Lett. **89**(9), 093103–093105 (2006).

Optical Materials EXPRESS

8. P. Spinelli, V. E. Ferry, J. van de Groep, M. van Lare, M. A. Verschuuren, R. E. I. Schropp, H. A. Atwater, and A. Polman, "Plasmonic light trapping in thin-film Si solar cells," J. Opt. **14**(2), 024002–024012 (2012).
9. K. Aydin, V. E. Ferry, R. M. Briggs, and H. A. Atwater, "Broadband polarization-independent resonant light absorption using ultrathin plasmonic super absorbers," Nat. Commun. **2**(1), 517 (2011).
10. I. Massiot, C. Colin, N. Pere-Laperne, P. Roca i Cabarrocas, C. Sauvan, P. Lalanne, J.-L. Pelouard, and S. Collin, "Nanopatterned front contact for broadband absorption in ultra-thin amorphous silicon solar cells," Appl. Phys. Lett. **101**(16), 163901 (2012).
11. C. Zhang, J. Gwamuri, S. Cvetanovic, M. Sadatgol, D. O. Guney, and J. M. Pearce, "Enhancement of hydrogenated amorphous silicon solar cells with front-surface hexagonal plasmonic arrays from nanoscale lithography," J. Opt. **19**(7), 075901 (2017).
12. V. L. Dalal, "Design considerations for a-Si solar cells," IEEE Trans. Electron Dev. **27**(4), 662–670 (1980).
13. E. Fortunato, D. Ginley, H. Hosono, and D. C. Paine, "Transparent Conducting Oxides for Photovoltaics," MRS Bull. **32**(03), 242–247 (2007).
14. A. Vora, J. Gwamuri, J. M. Pearce, P. L. Bergstrom, and D. Güney, "Multi-resonant silver nano-disk patterned thin film hydrogenated amorphous silicon solar cells for Staebler-Wronski effect compensation," J. Appl. Phys. **116**(9), 093103 (2014).
15. H. A. Atwater and A. Polman, "Plasmonics for improved photovoltaic devices," Nat. Mater. **9**(3), 205–213 (2010).
16. C. Algora and V. Diaz, "Influence of series resistance on guidelines for manufacture of concentrator p□on□n GaAs solar cells," Prog. Photovolt. Res. Appl. **8**(2), 211–225 (2000).
17. L. D. Nielsen, "Distributed series resistance effects in solar cells," IEEE Trans. Electron Dev. **29**(5), 821–827 (1982).
18. J. T. Lin, C. C. Lai, C. T. Lee, Y. Y. Hu, K. Y. Ho, and S. W. Haga, "A High-Efficiency HIT Solar Cell With Pillar Texturing," IEEE Journal of Photovoltaics **8**(3), 669–675 (2018).
19. M. Berginski, J. Hüpkes, W. Reetz, B. Rech, and M. Wuttig, "Recent development on surface-textured ZnO: Al films prepared by sputtering for thin-film solar cell application," Thin Solid Films **516**(17), 5836–5841 (2008).
20. J. Müller, B. Rech, J. Springer, and M. Vanecek, "TCO and light trapping in silicon thin film solar cells," Sol. Energy **77**(6), 917–930 (2004).
21. K. Nakayama, K. Tanabe, and H. A. Atwater, "Plasmonic nanoparticle enhanced light absorption in GaAs solar cells," Appl. Phys. Lett. **93**(12), 121904 (2008).
22. J. Yang, J. You, C. C. Chen, W. C. Hsu, H. R. Tan, X. W. Zhang, Z. Hong, and Y. Yang, "Plasmonic polymer tandem solar cell," ACS Nano **5**(8), 6210–6217 (2011).
23. M. T. Boyd, S. A. Klein, D. T. Reindl, and B. P. Dougherty, "Evaluation and validation of equivalent circuit photovoltaic solar cell performance models," J. Sol. Energy Eng. **133**(2), 021005 (2011).
24. System Advisor Model Version, 2017.9.5 (SAM 2017.9.5) Website. Simple Efficiency Module. National Renewable Energy Laboratory. Golden, CO. Accessed October 31, 2016. https://sam.nrel.gov/content/simple-efficiency-module.
25. N. Balasubramanian and A. Subrahmanyam, "Studies on evaporated indium tin oxide (ITO)/silicon junctions and an estimation of ITO work function," J. Electrochem. Soc. **138**(1), 322–324 (1991).
26. S. Y. Chou and W. Ding, "Ultrathin, high-efficiency, broad-band, omni-acceptance, organic solar cells enhanced by plasmonic cavity with subwavelength hole array," Opt. Express **21**(101 Suppl 1), A60–A76 (2013).
27. F. Burmeister, W. Badowsky, T. Braun, S. Wieprich, J. Boneberg, and P. Leiderer, "Colloid monolayer lithography-A flexible approach for nanostructuring of surfaces," Appl. Surf. Sci. **144**, 461–466 (1999).
28. C. Zhang, S. Cvetanovic, and J. M. Pearce, "Fabricating ordered 2-D nano-structured arrays using nanosphere lithography," MethodsX **4**, 229–242 (2017).
29. J. C. Hulteen, D. A. Treichel, M. T. Smith, M. L. Duval, T. R. Jensen, and R. P. Van Duyne, "Nanosphere lithography: size-tunable silver nanoparticle and surface cluster arrays," J. Phys. Chem. B **103**(19), 3854–3863 (1999).
30. M. R. Goncalves, "Plasmonic nanoparticles: fabrication, simulation and experiments," J. Phys. D Appl. Phys. **47**(21), 213001 (2014).
31. C. L. Haynes, and R. P. Van Duyne, "Nanosphere lithography: a versatile nanofabrication tool for studies of size-dependent nanoparticle optics," Journal of Physical Chemistry B **105**, 5599–5611 (2001).
32. J. Linnet, A. R. Walther, C. Wolff, O. Albrektsen, N. A. Mortensen, and J. Kjelstrup-Hansen, "Transparent and conductive electrodes by large-scale nano-structuring of noble metal thin-films," Opt. Mater. Express **8**(7), 1733–1746 (2018).
33. M. Kaniber, K. Schraml, A. Regler, J. Bartl, G. Glashagen, F. Flassig, J. Wierzbowski, and J. J. Finley, "Surface plasmon resonance spectroscopy of single bowtie nano-antennas using a differential reflectivity method," Sci. Rep. **6**(1), 23203 (2016).
34. J. Ziegler, L. Xia, R. Zejnelovic, and D. Borchert, "Changes in contact resistance of different metals to magnetron sputtered ITO while annealing." Proceeding of 25th EUPVSEC Valencia (2010).
35. A. Klöppel, W. Kriegseis, B. K. Meyer, A. Scharmann, C. Daube, J. Stollenwerk, and J. Trube, "Dependence of the electrical and optical behaviour of ITO–silver–ITO multilayers on the silver properties," Thin Solid Films **365**(1), 139–146 (2000).
36. H. Tian, F. Mancilla-David, K. Ellis, E. Muljadi, and P. Jenkins, "A cell-to-module-to-array detailed model for photovoltaic panels," Sol. Energy **86**(9), 2695–2706 (2012).

Optical Materials EXPRESS

37. J. Tatami, T. Katashima, K. Komeya, T. Meguro, and T. Wakihara, "Electrically conductive CNT□dispersed silicon nitride ceramics," J. Am. Ceram. Soc. **88**(10), 2889–2893 (2005).
38. F. Nehm, S. Schubert, L. Müller-Meskamp, and K. Leo, "Observation of feature ripening inversion effect at the percolation threshold for the growth of thin silver films," Thin Solid Films **556**, 381–384 (2014).
39. J. Gwamuri, A. Vora, J. Mayandi, D. O. Güney, P. L. Bergstrom, and J. M. Pearce, "A new method of preparing highly conductive ultra-thin indium tin oxide for plasmonic-enhanced thin film solar photovoltaic devices," Sol. Energy Mater. Sol. Cells **149**, 250–257 (2016).
40. M. T. García, I. Gracia, G. Duque, Ad. Lucas, and J. F. Rodríguez, "Study of the solubility and stability of polystyrene wastes in a dissolution recycling process," Waste Manag. **29**(6), 1814–1818 (2009).
41. H. Chandra, S. W. Allen, S. W. Oberloier, N. Bihari, J. Gwamuri, and J. M. Pearce, "Open-source automated mapping four-point probe," Materials (Basel) **10**(2), 110 (2017).
42. N. G. Patel, P. D. Patel, and V. S. Vaishnav, "Indium tin oxide (ITO) thin film gas sensor for detection of methanol at room temperature," Sens. Actuators B Chem. **96**(1–2), 180–189 (2003).
43. Y. H. Tak, K. B. Kim, H. G. Park, K. H. Lee, and J. R. Lee, "Criteria for ITO (indium–tin-oxide) thin film as the bottom electrode of an organic light emitting diode," Thin Solid Films **411**(1), 12–16 (2002).